High-sensitivity crossed-resonator laser apparatus for improved tests of Lorentz invariance and of space-time fluctuations

Q. Chen,[†] E. Magoulakis, and S. Schiller[*]

Institut für Experimentalphysik, Heinrich-Heine-Universität Düsseldorf, 40225 Düsseldorf, Germany

(Received 4 August 2015; published 27 January 2016)

We describe an improved Michelson-Morley-type laser apparatus for highly sensitive tests of Lorentz invariance in the electron and photon sectors. The realization of an ultrastable rotation table reduced by more than one order systematic effects occurring with the rotation period. We also reduced by one order the noise level, resulting in integration times smaller by more than one order. Under reasonable assumptions, we determine five coefficients of the standard model extension test theory, with uncertainties similar to the previous best experiments, but with a 30 times shorter data acquisition time span. Four coefficients are consistent with zero at the $(4\text{–}8) \times 10^{-18}$ level, while one, $(\tilde{\kappa}_{e-})^{ZZ} \simeq 5 \times 10^{-17}$, appears to be caused by unidentified systematic effects. In addition, the apparatus' performance leads to a limit for the strength of (hypothetical) space-time fluctuations improved by a factor of 3.7.

DOI: 10.1103/PhysRevD.93.022003

I. INTRODUCTION

Tests of Lorentz invariance are of great interest in the field of fundamental physics. Not only has a significant variety of experiments been performed in the last decade [1], but the breadth of types of Lorentz invariance violation effects undergoing tests is continuing to increase [2]. These tests address different species of particles (photons, electrons, positrons, nuclei, atoms, and subatomic particles).

Lorentz invariance related to photon propagation can be tested using resonators, in a generalization of the original Michelson-Morley experiment. The test consists in verifying the independence of a resonator's optical resonance frequency from its orientation in space. While such experiments can be performed in the microwave domain (see Ref. [3] and references therein) or in the optical domain [4–11], in recent years, the optical approach has become the more sensitive one. The most recent experiments were performed with blocks of ultra-low-expansion (ULE) glass, which house two orthogonal resonators. The first such device was reported on in Ref. [9]. Resonators are generally solids, and thus the dynamics of the electrons therein is responsible for the structure of the solid, in particular for the distance between the mirrors of the resonator. Therefore, a test using an electromagnetic resonator addresses the behavior of both photons and electrons. A global interpretation of such tests in the framework of the Standard Model extension (SME) test theory has been worked out [12,13].

In the present paper, we report on the exploration of approaches for improvement in sensitivity of a resonator-based experiment and on the limitations encountered. We present the improvements of the apparatus of Ref. [10] and Lorentz invariance results achieved with it. In addition, we show that the increased sensitivity also allows reducing the upper limit of the strength of hypothetical space-time fluctuations [14]. We also point to the future approaches toward the reduction of systematic effects, potentially enabling new performance levels.

II. OVERVIEW OF THE APPARATUS AND ITS MAIN PROPERTIES

A. Optical system

The main changes of the system described in Ref. [10] included modifications of the reference cavities, of the optics setup, and of the tilt stabilization control system. We discuss them in turn.

The mirrors of the two cavities (cavity lengths are 8.4 cm) were changed from ULE glass substrate material to fused silica, which reduces the calculated thermal noise limit of each cavity from 1.0×10^{-15} to 4.6×10^{-16} (Allan deviation normalized to resonance frequency). We also optically contacted ULE glass rings to the cavity mirrors for reduction of the cavities' coefficients of thermal expansion [15]. The finesse of the cavities with the new mirrors is approximately 520,000.

The schematic of the optical setup is shown in Fig. 1. A single Nd:YAG laser (1064 nm, $\nu_0 \simeq 2.8 \times 10^{14}$ Hz) is used. Not only the cavity block itself but also the optical setup to couple the laser wave into the cavities are located in a vacuum chamber, following our approach described in Ref. [16]. After passing through a first acousto-optic modulator [(AOM1) driven by the second direct digital synthesizer (DDS2) at a fixed frequency but variable amplitude], the first-order diffracted laser beam (ν_1) is split into two paths. One path is sent through a second acousto-optic modulator [(AOM2) driven by DDS3], where the first-order wave is frequency-shifted by approximately 230 MHz,

[*]step.schiller@hhu.de

[†]Present address: State Key Laboratory of Magnetic Resonance and Atomic and Molecular Physics, Wuhan Institute of Physics and Mathematics, Chinese Academy of Sciences, Wuhan 430071, China.

 © 2016 American Physical Society

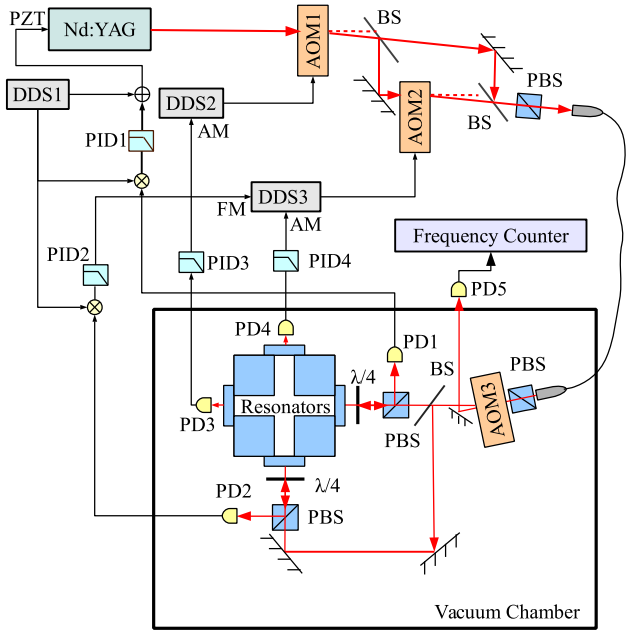

FIG. 1. Schematic of the optical setup. Nd:YAG, nonplanar ring oscillator Nd:YAG laser (1064 nm); DDS, direct digital synthesizer; PZT, piezoactuator input of the Nd:YAG laser; AOM, acousto-optic modulator; BS, beam splitter; PBS, polarizing beam splitter; $\lambda/4$, quarter-wave plate; PD, photodetectors; PID, proportional-integral-derivative circuits; FM, frequency modulation input; AM, amplitude modulation input. The Nd:YAG laser temperature is also regulated, using the integral of error signal 1 (not shown). Error signal 1 is produced by PID1.

resulting in ν_2. This value is the frequency difference between the nearby fundamental modes TEM_{00} of the two cavities. The two laser beams (frequencies ν_1, ν_2) are then combined again, collected by a fiber collimator, and sent into the vacuum chamber via optical fiber. There, the wave output from the fiber is split again, and the two parts are coupled to the fundamental modes of the two orthogonal cavities. The wave without a frequency shift (ν_1) is frequency locked to the cavity by feedback to the piezoactuator (PZT) input of the laser. The wave with frequency shift (ν_2) is frequency locked to the other cavity of the block by feedback to the frequency modulation input (FM) of DDS3. Note that both waves reach each resonator and each photodetector PD1 and PD2. The error signals for the frequency stabilization are generated using the Pound-Drever-Hall method and the two feedback signals are produced by PID1 and PID2, respectively. The frequency modulations for both error signals are generated by modulating the PZT of the laser at 4.8 MHz (DDS1). Using the same frequency modulation to generate the error signals for both lasers, an approximately symmetric splitting of the laser power at the beam splitter after AOM3, and similar incoupling levels into the cavities, leads to the residual amplitude modulation (RAM) effect being substantially in the common mode for the two frequency locks and to a corresponding substantial, albeit not perfect, cancellation in the beat frequency.

Two photodetectors (PD3 and PD4) monitor the laser powers transmitted through the cavities, and the respective signals are used to stabilize the laser power in the cavities by controlling the rf powers delivered to AOM1 and AOM2 by their drivers DDS1 and DDS3. A fast photodetector (PD5) placed outside of the chamber is used to monitor the beat frequency $\Delta\nu = |\nu_1 - \nu_2|$ between the two lasers.

B. Tilt stabilization

The stabilization of the tilt of the system is an improved version of Ref. [10] and includes two parts. The stationary part is a granite plate which is supported and controlled by high-pressure air actuators to the level of ± 5 μrad long term. The rotating part consists of a cross-shaped frame on which rests an active vibration isolation system that supports an optical breadboard. The tilt of this breadboard is measured by two sensors fixed to this optical breadboard and oriented in orthogonal directions X, Y. The tilt is actively controlled by voice coil actuators. Compared with the tilt stabilization used in our previous setup, the improvements of the system include, first, a high reading rate of the tilt sensor signals by the data acquisition card (DAQ), which reduces DAQ readout noise much below the noise of the tilt signals. The control signals for the voice coil actuators of the breadboard are filtered by concatenation of three digital proportional-integral-derivative controllers with feedback rates of 15 Hz. By fitting a function to the variation of the voice coil control signal with the rotation angle, we obtain the absolute tilt of the granite plate as a function of the rotation angle. By comparing this absolute tilt with the tilt error monitored by the tilt controller of the granite plate, the set point of the tilt of granite plate is set to zero absolute tilt, i.e., normal to local acceleration.

The whole setup is housed within a frame covered with thin metal plates, which reduces the influence of air fluctuations on the tilt stability of the rotation table and keeps the setup at a moderate temperature (25 °C).

III. CHARACTERIZATION OF THE APPARATUS

A. Generalities

To characterize the instability of or systematic effects on a generic parameter p (beat frequency, tilt, etc.) as a function of time t, we can compute its Allan deviation $\sigma_p(\tau)$ (τ is the averaging time) and model the time series $p(t)$ as being correlated to rotation, according to

$$\begin{aligned} p(t) = {} & A_p(t_i) + a_p(t_i)(t-t_i) + b_p(t_i)(t-t_i)^2 \\ & + c_p(t_i)(t-t_i)^3 + 2B_p(t_i)\sin(2\omega_{rot}t) \\ & + 2C_p(t_i)\cos(2\omega_{rot}t) + 2D_p(t_i)\sin(\omega_{rot}t) \\ & + 2E_p(t_i)\cos(\omega_{rot}t), \end{aligned} \tag{1}$$

with t_i the starting time of a particular time interval, $A_p(t_i)$ a slowly varying offset, and $\omega_{\mathrm{rot}} = 2\pi/60$ s the rotation

angular frequency of the table used in the present experiment. a_p, b_p, and c_p are slowly varying functions that describe the time drift. In the case $p = \Delta\nu$, they describe the effects of thermal expansion and dimensional relaxation of the cavities. B_p, C_p, D_p, and E_p are the modulation (half-)amplitudes due to systematic effects correlated with rotation, or due to Lorentz invariance violation. The addition of terms oscillating with $3\omega_{rot}$ and $4\omega_{\rm rot}$ to Eq. (1) leads to insignificant changes in the results given in Sec. IV B. Nevertheless, such modulations are present in the data and are discussed further below.

Some characterizations were also performed when the table was not rotating, in order to compare with the rotating case. In that case, the time series of the frequency is fitted by the same expression above.

When p is a parameter that is actively controlled to remain stable in time, such as a tilt, the drift terms involving a_p, b_p, and c_p are set to zero before fitting.

To analyze a time series $p(t)$, we divide it into intervals of ten rotations each, i.e., into intervals of 10 min duration, and fit expression Eq. (1) to each interval. For display purposes only, the resulting list of fit parameters $p_{\rm mod} = \{B_p(t_i), C_p(t_i), D_p(t_i), E_p(t_i)\}$ is binned with respect to 10-min-long sidereal time intervals ($t_\oplus$) modulo 1 sidereal day. The average of the values in each time bin k, $\langle\{B_p\}_k\rangle$, etc., and the standard deviation of the values, $\sigma(\{B_p\}_k)$, etc., are computed and displayed in some figures below.

Furthermore, we fit each time series $p_{\rm mod}$ according to a time dependence suggested by the Roberston-Mansouri-Sexl (RMS) and SME test theories [17,18] (see also the Appendix),

$$\begin{aligned} B_p(t_i) = {} & B_{p,0}(t_\oplus) + B_{p,1}(t_\oplus)\sin(\omega_\oplus t_\oplus) \\ & + B_{p,2}(t_\oplus)\cos(\omega_\oplus t_\oplus) + B_{p,3}(t_\oplus)\sin(2\omega_\oplus t_\oplus) \\ & + B_{p,4}(t_\oplus)\cos(2\omega_\oplus t_\oplus), \end{aligned} \tag{2}$$

and correspondingly for C_p, D_p, E_p. $t_\oplus$ is the sidereal time corresponding to the time t_i. The quantities $B_{p,n}$, $C_{p,n}$, $D_{p,n}$, and $E_{p,n}$ may be called sidereal modulation coefficients.

When p is the fractional beat frequency deviation $y = \Delta\nu/\nu_0$, the RMS and SME test theories state that each amplitude function $C_{y,n}(t_\oplus)$ is a sum of a constant term and sine/cosine modulation terms at the Earth's orbital frequency, thus they vary slowly in time. The same is the case for the $B_{y,n}(t_\oplus)$, except for $B_{y,0}$, which is zero. For the amplitudes D_ν, E_ν as well as for other physical parameters p, Eq. (2) provides a convenient qualitative description, without implying a fundamental physics interpretation such as a test theory.

B. Tilt

Figure 2 shows the Allan deviation of the sensor readings θ_X and θ_Y during tilt stabilization. At 30 s integration time,

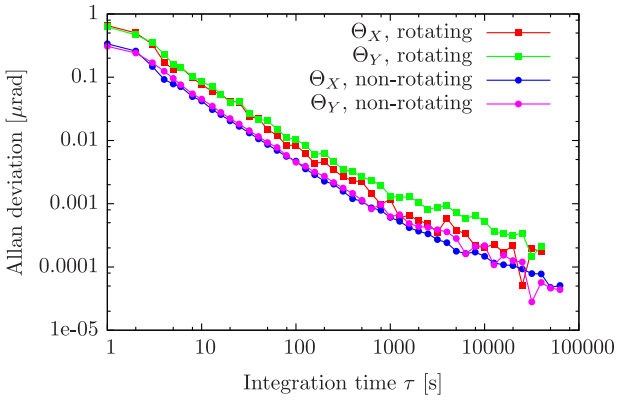

FIG. 2. Allan deviation of the table tilts under nonrotating and rotating conditions.

under rotation, the values are $\sigma_{\Theta X}$, $\sigma_{\Theta Y} \simeq 30$ nrad, only approximately a factor 2 higher than in the absence of rotation. For comparison, in our previous system, they were 0.7 and 1.2 μrad [9], i.e., factors 25 and 40 higher, respectively.

Table I summarizes the sidereal modulation coefficients under active control. In the absence of rotations, the coefficients are all consistent with zero, within their respective statistical errors, which lie in the range 0.03 to 0.05 nrad. Under rotation, the tilt compensation remains very high: the sidereal coefficients related to $B_{\theta X}(t_i)$, $B_{\theta Y}(t_i)$, $C_{\theta X}(t_i)$, and $C_{\theta Y}(t_i)$ are not larger than 5 nrad, while those related to $D_{\theta X}(t_i)$, $D_{\theta Y}(t_i)$, $E_{\theta X}(t_i)$, and $E_{\theta Y}(t_i)$ do not exceed 0.7 nrad. The (time-independent) modulation coefficients $B_{\theta X,0}(t_i)$, $B_{\theta Y,0}(t_i)$, $C_{\theta X,0}(t_i)$, and $C_{\theta Y,0}(t_i)$ are relatively large when rotation occurs. This is due to the shape of the support of the rotating part, a cross. This leads to a back action on the granite support with a period equal to half the rotation period (angular frequency $2\omega_{\rm rot}$) and is directly observable by the tilt sensors attached to the granite support. It was not possible, in our apparatus, to compensate this effect by adjusting the tilt of the granite plate or the load distribution of the rotating part.

Considering the tilt sensitivity of the cavities, we find that the tilt stabilization performance is sufficient. The sensitivity of the cavity frequency difference on the tilt was measured to be < 50 mHz/μrad ($< 2 \times 10^{-10}$/rad) for tilts around the X– and Y–directions. From this, we deduce that the systematic effect of tilt on the fractional frequency deviation $y = \Delta\nu/\nu_0$, i.e., of $B_{\theta,0}(t_i)$ on $B_y(t_i)$ and of $C_{\theta,0}(t_i)$ on $C_y(t_i)$, is less than 50 mHz/μrad × 5 nrad/$\nu_0 \simeq 0.9 \times 10^{-18}$. This level is much smaller than the deviations of the mean values $\langle B_{y,0}(t_i)\rangle$ and $\langle C_{y,0}(t_i)\rangle$ from zero (see below) and therefore cannot explain the latter.

C. Angular rotation speed

The angular rotation speed was characterized. All sidereal coefficients $B_{\omega_{rot},n}$, $C_{\omega_{rot},n}$, $D_{\omega_{rot},n}$, and $E_{\omega_{rot},n}$

TABLE I. The sidereal coefficients of the table tilts θ_X, θ_Y under nonrotating (NR) and rotating (R) conditions. The units are nrad.

		n				
Coefficient		0	1	2	3	4
$B_{\Theta X,n}$	R	1.38 ± 0.04	-0.40 ± 0.06	-0.05 ± 0.06	-0.13 ± 0.06	-0.07 ± 0.06
	NR	-0.02 ± 0.02	0.02 ± 0.03	-0.02 ± 0.03	0.04 ± 0.03	0.01 ± 0.03
$C_{\Theta X,n}$	R	4.80 ± 0.04	0.05 ± 0.06	0.11 ± 0.06	0.07 ± 0.06	-0.01 ± 0.06
	NR	0.00 ± 0.03	-0.03 ± 0.04	-0.06 ± 0.04	0.03 ± 0.04	-0.04 ± 0.04
$D_{\Theta X,n}$	R	0.22 ± 0.03	-0.06 ± 0.04	0.18 ± 0.04	-0.09 ± 0.04	-0.01 ± 0.04
	NR	-0.02 ± 0.02	0.02 ± 0.02	0.00 ± 0.02	0.01 ± 0.02	-0.01 ± 0.02
$E_{\Theta X,n}$	R	-0.21 ± 0.03	0.01 ± 0.04	0.31 ± 0.04	0.03 ± 0.04	0.03 ± 0.04
	NR	0.01 ± 0.02	-0.02 ± 0.02	-0.02 ± 0.03	0.00 ± 0.02	-0.01 ± 0.02

		n				
Coefficient		0	1	2	3	4
$B_{\Theta Y,n}$	R	3.56 ± 0.06	0.13 ± 0.09	0.08 ± 0.09	-0.04 ± 0.09	-0.03 ± 0.09
	NR	0.02 ± 0.03	0.05 ± 0.05	-0.05 ± 0.05	-0.05 ± 0.05	0.00 ± 0.05
$C_{\Theta Y,n}$	R	-0.74 ± 0.06	0.39 ± 0.09	0.15 ± 0.09	0.08 ± 0.09	0.07 ± 0.09
	NR	0.04 ± 0.04	0.05 ± 0.05	-0.02 ± 0.05	0.02 ± 0.05	-0.04 ± 0.05
$D_{\Theta Y,n}$	R	0.40 ± 0.04	-0.08 ± 0.05	0.37 ± 0.05	-0.03 ± 0.05	0.11 ± 0.05
	NR	-0.01 ± 0.02	-0.01 ± 0.03	-0.02 ± 0.03	0.00 ± 0.03	-0.03 ± 0.03
$E_{\Theta Y,n}$	R	0.61 ± 0.04	0.05 ± 0.06	-0.14 ± 0.06	0.08 ± 0.06	-0.03 ± 0.06
	NR	0.02 ± 0.02	-0.04 ± 0.03	0.01 ± 0.03	0.00 ± 0.03	0.00 ± 0.03

are compatible with zero. The largest statistical standard error of any coefficient is 4 μdeg/s. In our previous work, we measured a beat frequency change of 0.6 Hz for a rotation speed change of 0.4 deg/s, at a rotation speed of 4 deg/s. Thus, the observed variations in the angular rotation speed do not have an appreciable effect on the beat frequency variations.

D. Cavity frequency difference

A typical behavior of the frequency difference $\Delta\nu(t)$ under rotation is shown in Fig. 3. Because there is no temperature for which the cavity difference is insensitive to temperature [9], residual temperature variations lead to a slow change in $\Delta\nu$. In addition, there is a contribution from the differential creep of the cavities. After removing the linear frequency drift from the data, we find the Allan deviation shown in Fig. 3, bottom. It exhibits a flat plateau extending from integration times of 2 s to approximately 100 s, with values $\simeq$0.22 Hz. Referred to a single cavity, this value is to be divided by $\sqrt{2}$, yielding 0.14 Hz, or 5.0×10^{-16} in fractional terms. This value is in good agreement with the calculated thermal noise limit mentioned above. For comparison, in the previous version of the experiment, we achieved a minimum of 1.7×10^{-15} (referred to a single cavity), however, increasing to 5×10^{-15} already at 30 s integration time. Figure 4 also reports the "best" 2.5-h-long data from the chosen 1 day measurement run, in which the deviations of $\Delta\nu(t)$ from linear-in-time drifting values were smallest. One can see that most of the beat frequency data deviated less than $\pm$1.5 Hz, or 5×10^{-15} in fractional terms.

The intrinsic noise of the apparatus is best studied in the absence of rotation. Figure 5 shows histograms of the

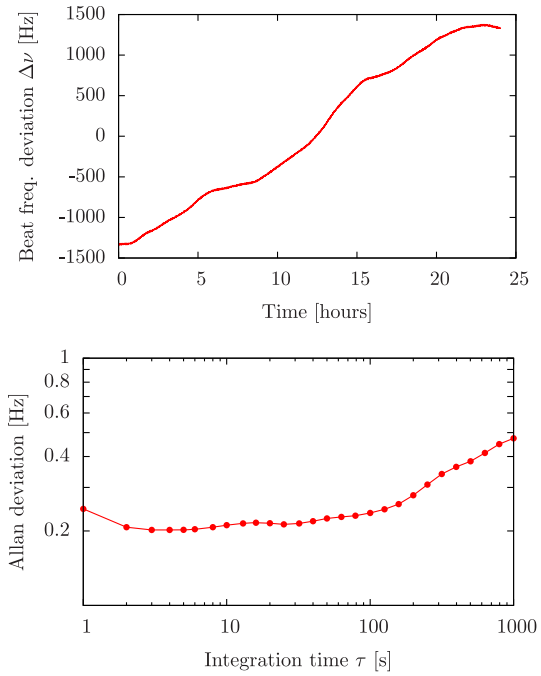

FIG. 3. Example of the long-term behavior of the cavity frequency difference $\Delta\nu(t)$. Top: beat frequency over a time interval of approximately 1 day. Bottom: the Allan deviation $\sigma_{\Delta\nu}(\tau)$, after removing the time-linear drift. The apparatus is rotating.

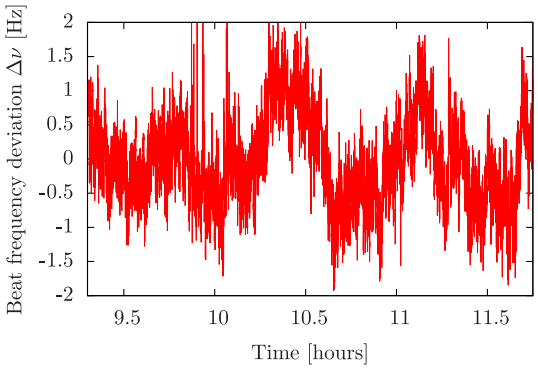

FIG. 4. A 2.5 h time interval of the beat frequency exhibiting a particularly constant drift (39 mHz/s), which was removed before plotting. One frequency reading per second is displayed. The apparatus is rotating.

amplitudes $B_y(t_i)$ and $C_y(t_i)$ of a data set including 25,800 considered pseudorotations spanning 430 h. Their mean values are compatible with zero, and their standard deviations are $\sigma(\{B_y(t_i)\}) = 7.2 \times 10^{-17}$, $\sigma(\{C_y(t_i)\}) = 7.1 \times 10^{-17}$. These standard deviations (after multiplication by 2 since B_y and C_y are half-amplitudes) indicate the fundamental sensitivity of the apparatus: they imply that resolving a Lorentz invariance violation at a 3σ level of 5×10^{-19} would require at least $(3 \times 2 \times 7 \times 10^{-17}/5 \times 10^{-19})^2 \simeq 0.7$ million rotations, or 2.2 years of uninterrupted rotation. This would still be feasible, considering realistic duty cycles.

The sidereal time dependence of the nonrotating noise is displayed in Figs. 6 and 7, and the associated sidereal coefficients are reported in Table II.

A clear indication of how insensitively the apparatus as a whole reacts under rotation is provided by the values of the amplitudes D_y and E_y, which describe effects occurring *at the rotation frequency*, when the apparatus is rotating. In an apparatus devoted to implementing a Lorentz invariance test at a desired level of sensitivity, their average values should be compatible with zero. The data set we analyze here and further below comprises 16,130 rotations over 269 h, centered around January 31, 2015. The time dependencies of D_y and E_y are shown in Fig. 8. The mean

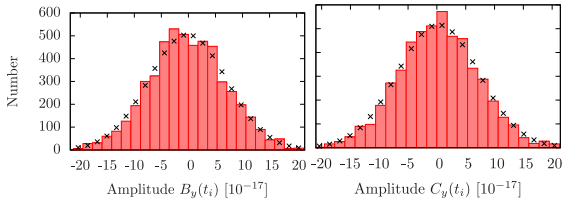

FIG. 5. Histograms of the beat frequency amplitudes $B_y(t_i)$ and $C_y(t_i)$ for the *nonrotating* apparatus. For comparison, the crosses indicate the histogram values of a Gaussian distribution with the same mean and variance as the corresponding data set.

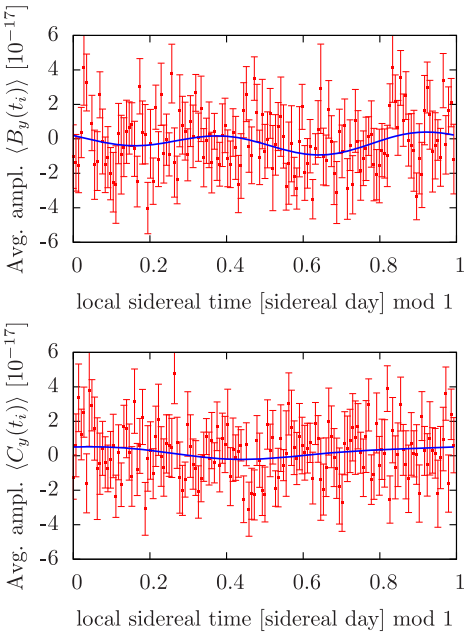

FIG. 6. Time analysis of the beat frequency amplitudes $B_y(t_i)$ and $C_y(t_i)$ for the nonrotating apparatus. Points: mean values $\langle B_y(t_i)\rangle_{\mathrm{sid},10}$ and $\langle C_y(t_i)\rangle_{\mathrm{sid},10}$ of the modulation amplitudes measured within 10 min intervals during each sidereal day. The error bars indicate the statistical standard errors of these mean values. Full line (blue): fit according to Eq. (2).

values are $\langle D_y(t_i)\rangle = (3.06 \pm 0.26) \times 10^{-17}$ and $\langle E_y(t_i)\rangle = (4.81 \pm 0.25) \times 10^{-17}$, which are not compatible with zero. This shows that some systematic effects are not fully suppressed at the high level of sensitivity achieved here.

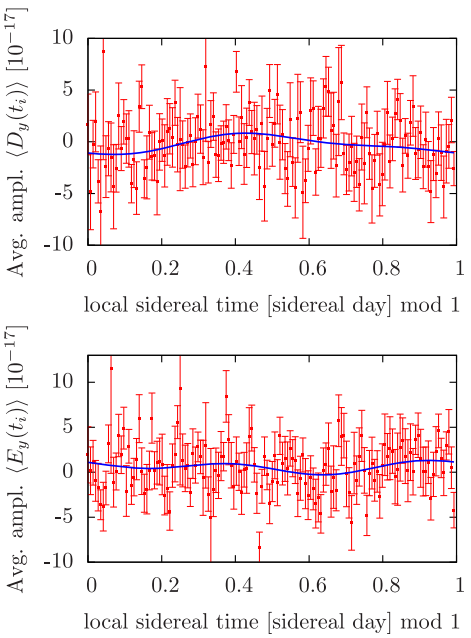

FIG. 7. Time analysis of the beat frequency amplitudes $D_y(t_i)$ and $E_y(t_i)$ for the nonrotating apparatus. See the caption of Fig. 6 for explanations.

TABLE II. The fit parameters of the beat frequency modulation amplitudes, according to Eq. (2), for the nonrotating apparatus. The units are 10^{-17}.

	n				
	0	1	2	3	4
$B_{y,n}$	-0.20 ± 0.14	0.21 ± 0.20	0.20 ± 0.19	-0.31 ± 0.19	0.34 ± 0.20
$C_{y,n}$	0.20 ± 0.13	-0.03 ± 0.19	0.34 ± 0.19	0.05 ± 0.19	-0.06 ± 0.19
$D_{y,n}$	-0.25 ± 0.22	-0.16 ± 0.31	-0.86 ± 0.31	-0.25 ± 0.31	0.20 ± 0.31
$E_{y,n}$	0.59 ± 0.21	0.27 ± 0.30	0.30 ± 0.30	-0.35 ± 0.29	0.37 ± 0.30

Nevertheless, the systematic effects correlated to complete rotations have been reduced to the noteworthy level of $< 1 \times 10^{-16}$ in fractional terms (again, $\langle D_y \rangle$, $\langle E_y \rangle$ must be multiplied by 2). For our experiment, this represents a significant improvement compared to the previous version [10], where the beat frequency modulation had an amplitude of approximately 3×10^{-15}. The current level of D_y- and E_y-related systematics is, however, higher than for B_y and C_y.

IV. TEST OF LORENTZ INVARIANCE

A. Properties of the data

The rotation data are displayed in Figs. 9 and 10. The mean values of the data are $\langle B_y(t_i) \rangle = (1.01 \pm 0.16) \times 10^{-17}$ and $\langle C_y(t_i) \rangle = (0.71 \pm 0.16) \times 10^{-17}$. The standard deviations of the data are 6.6×10^{-17} and 6.8×10^{-17}, respectively. The reason for the difference of these standard deviations as compared to the nonrotating case could not be determined; it may be due slightly different environmental conditions. Our previous result [10] was mean values $\langle B_y(t_i) \rangle = (1.7 \pm 0.2) \times 10^{-17}$ and $\langle C_y(t_i) \rangle = (0.2 \pm 0.2) \times 10^{-17}$ and standard deviations of

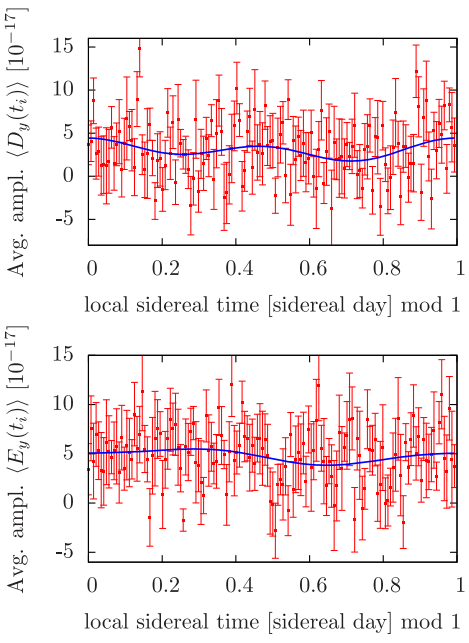

FIG. 8. Time analysis of the beat frequency amplitudes $D_y(t_i)$ and $E_y(t_i)$ for the *rotating* apparatus. See the caption of Fig. 6 for explanations.

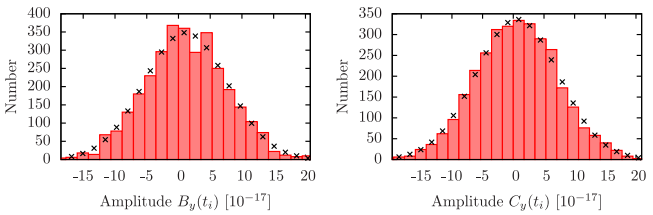

FIG. 9. Histograms of the amplitudes $B_y(t_i)$ and $C_y(t_i)$ for the rotating apparatus. For comparison, the crosses indicate the histogram values of a Gaussian distribution with the same mean and variance as the corresponding data set.

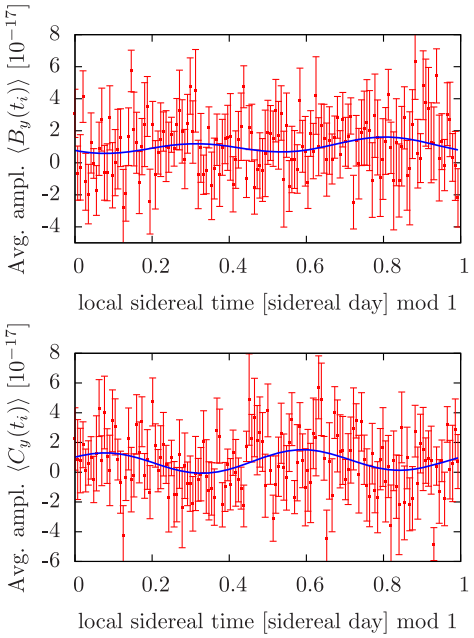

FIG. 10. Time analysis of the amplitudes $B_y(t_i)$ and $C_y(t_i)$ for the rotating apparatus. Points: mean values of the modulation amplitudes measured within 10 min intervals during each sidereal day. The error bars indicate the statistical standard errors of the means. Full line (blue): fit according to Eq. (2).

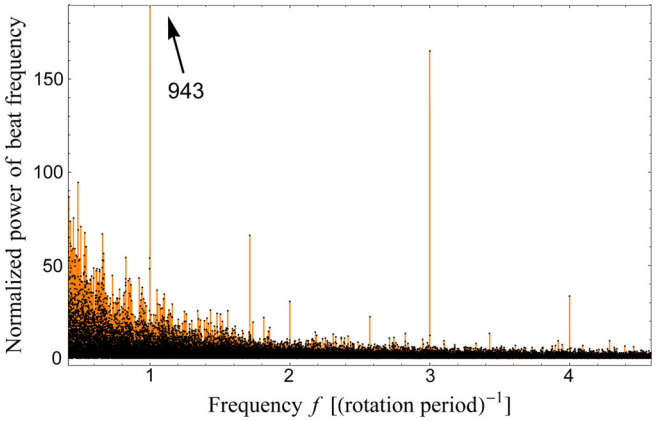

FIG. 11. Periodogram of the full, detrended beat frequency data. Note that the periodogram shows the power of the signal and is normalized to the variance of the data.

the data 7.5×10^{-16} and 6.1×10^{-16}, respectively. Thus, we see that we reduced the fluctuations of the data by approximately a factor of 10. The uncertainties of the means in the new measurement are nearly the same as previously, even though the data comprise approximately 11 times fewer rotations, obtained with just 11.2 days of data, as compared to 240 days of data acquired over a time span of 13 months previously.

We have performed a Lomb-Scargle periodogram analysis of the beat frequency data. For this purpose, each 10 min beat frequency data interval was first fitted according to Eq. (1). Then, the determined linear, quadratic, and cubic drift contributions were removed from the data. All detrended data intervals were joined into a global time series on which the analysis was performed.

The periodogram (Fig. 11) shows modulations at ω_{rot}, $2\omega_{\mathrm{rot}}$, $3\omega_{\mathrm{rot}}$, and $4\omega_{\mathrm{rot}}$. The modulation power at $\omega = 2\omega_{\mathrm{rot}}$ is very small, within an order of magnitude of the noise level at that frequency. We stress that (within the current test theories) only the $2\omega_{\mathrm{rot}}$ signal can be due to a Lorentz violation. The other modulation components are necessarily caused by systematic effects. In particular, the strength of the $4\omega_{\mathrm{rot}}$ signal, the harmonic of $2\omega_{\mathrm{rot}}$, is a systematic whose the strength can be taken as one of the indicators of how sensitive the apparatus is to disturbances.

The fitted sidereal modulation coefficients relevant for determining violation coefficients according to the RMS or SME test theory are given in Table III, and the fits are shown as lines in Fig. 10. The sidereal coefficients have statistical errors that are approximately ten times smaller than in our previous work. Again, this attests to the improved sensitivity of the new apparatus. We may state this sensitivity as 1.4×10^{-17} after 12 days of integration time (this value is the 3σ uncertainty of the $2B_{y,n>0}$ and $2C_{y,n>0}$ coefficients, according to Table III).

Among $B_{y,1}$, $B_{y,2}$, $C_{y,1}$, and $C_{y,2}$, the latter has the largest value, nearly 3σ in magnitude. To characterize the relevance of this value, a more extended analysis of the data was done by computing the harmonic-content periodograms of B_y and C_y [19]. In this analysis, fits of the data with periodic functions having a fundamental frequency ω and a second harmonic 2ω are performed, wherein ω was chosen to lie in the range $\omega \in [0.5\omega_\odot, 1.5\omega_\odot]$ (the precise values of these limits are arbitrary). It was found that $\omega = \omega_\odot$ does not stand out as having a particularly low χ^2 fit error. Several values $\omega \neq \omega_\odot$ yield χ^2 fit errors comparable to or smaller than the case $\omega = \omega_\odot$. The presence of (noise or signal) peaks of comparable strength at frequencies that are unrelated to the frequency characteristic of Lorentz invariance violation makes it doubtful that $C_{y,2}$ constitutes a clear Lorentz violation signal. In addition, its value reduces to 2σ if 1 day of data is removed. The harmonic-content periodgram analysis of the data taken under nonrotating conditions provides a useful comparison.

The sidereal coefficients $B_{y,0}$ and $C_{y,0}$ are statistically significantly different from zero by approximately 6σ. Note that the values of $B_{y,0}$ and $C_{y,0}$ are approximately 7 and 9 times smaller, respectively, than the standard deviation *of the data*. Therefore, they distinctly emerge from the noise only after averaging over several hundred ten-rotation intervals, i.e., over a few days.

However, we believe that the evidence for a Lorentz invariance violation is not sufficiently strong. While the power of the $4\omega_{\mathrm{rot}}$ signal is particularly small in comparison to other runs, it is still clearly above the noise and comparable in strength to the $2\omega_{\mathrm{rot}}$ signal. Because of the presence of this systematic, we cannot exclude that the $2\omega_{\mathrm{rot}}$ signal is also due to (the same) systematics, and so are all sidereal modulation coefficients and the RMS and SME parameters to be discussed in the following. Moreover, we find that small changes in the apparatus (which lead to significant changes in the $4\omega_{\mathrm{rot}}$ signal power, as well as in the magnitudes of $D_{y,0}$ and $E_{y,0}$) lead to changes in $B_{y,0}$ and

TABLE III. The fit parameters of the modulation half-amplitudes $B_y(t_i)$ and $C_y(t_i)$, according to Eq. (2), for the rotating apparatus. The units are 10^{-17}.

	n				
	0	1	2	3	4
$B_{y,n}$	1.02 ± 0.16	0.03 ± 0.23	-0.21 ± 0.23	0.05 ± 0.23	0.37 ± 0.23
$C_{y,n}$	0.72 ± 0.17	0.08 ± 0.23	-0.12 ± 0.23	-0.31 ± 0.23	-0.62 ± 0.23

$C_{y,0}$ which are larger than the above values. This is an indication that, at the level of the above values, systematic effects can be a significant contribution.

B. Interpretation of the data

1. SME test theory

The SME applied to cavities [18] also leads to the prediction Eq. (2) with again $B_{y,0} = 0$ and the functions $B_{y,n}$ essentially determined by the functions $C_{y,n}$. Each amplitude function $C_{y,n}(t_\oplus)$ is a sum of a constant term and a modulation term with period of 1 sidereal year. Assuming Lorentz invariance holds for the electron, the amplitudes of the modulation terms are proportional to combinations of the three off-diagonal elements of the electromagnetic SME coefficient matrix $(\tilde{\kappa}_{o+})$ and suppressed by a factor $\approx 10^{-4}$ (ratio of Earth orbital velocity and speed of light). The constant terms are each linear combinations of one of the former and one of five coefficients of the SME matrix $(\tilde{\kappa}_{e-})$. As the present data set is short compared to 1 year, the $C_{y,n}(t_\oplus)$ are nearly time independent, and thus the eight relevant elements of $(\tilde{\kappa}_{o+})$ and $(\tilde{\kappa}_{e-})$ cannot all be independently determined. Instead, a simplified case may be considered. We assume that the SME coefficients $\tilde{\kappa}_{o+}$ are smaller than 5×10^2 times the smallest relevant element of the $(\tilde{\kappa}_{e-})$ matrix so that they may be neglected. The very strong astrophysical bounds on $\tilde{\kappa}_{o+}$ [20] justify this assumption.

Five SME $(\tilde{\kappa}_{e-})$ coefficients (or combinations) can then be determined, each being proportional to a $C_{y,n}$ sidereal coefficient, with factors depending on the latitude of the laboratory. In the fit, we again introduce a free parameter, $B_{y,0,\mathrm{syst}}$, in Eq. (2) so as to account for the experimentally observed nonzero value $B_{y,0}$. The results of the fit are given in Table IV.

The value of $(\tilde{\kappa}_{e-})^{ZZ}$ is nonzero but, as described above, is believed to be due to systematic effects. The other values are consistent with zero.

V. TEST OF SPACE-TIME FLUCTUATIONS

In Ref. [21], it has been argued that the strength of the fluctuations of the beat of two lasers locked to two different cavities can be interpreted as bounding the strength of hypothetical fluctuations of space-time. The limits can be improved with new generations of cavity experiments. Of course, even if all technical noise sources have been minimized, the Brownian noise of the cavities and quantum noise of the readout will pose a fundamental limit to the sensitivity of such a test.

We can use data obtained with our apparatus to set new limits. In our apparatus, the two cavities are oriented orthogonal to each other, and therefore the fluctuations of space-time as probed by the laser beams circulating in them could conceivably be uncorrelated. Obviously, if we are interested in fluctuations occurring at a Fourier frequency f, the apparatus should rotate with period $T \gg 1/f$, or not rotate at all.

From nonrotating data, we have chosen a 2.5 h interval in which the deviations of $\Delta\nu(t)$ from a constant drift rate were the smallest. The power spectral density of this data set (with the time-linear drift removed), normalized to the laser frequency ν_0 and divided by a factor of 2 (to account for the two cavities presumably having uncorrelated space-time fluctuations), is shown in Fig. 12 as a brown curve. For comparison, the orange curve shows the spectral density of a data subset of particularly high stability for the rotating apparatus, shown in Fig. 4. We see that the two cases have similar noise levels. The peak at the frequency $(40\ \mathrm{s})^{-1}$ in the rotating case is not at $(2\pi)2\omega_{\mathrm{rot}}$ and appears to be spurious. Taking into account the confidence level of the computed spectral density as in Ref. [21], we obtain an upper limit for space-time fluctuations with f^{-1} dependence, $S(f) = 1.9 \times 10^{-31}/f$ (95% confidence interval). It is shown as a black line in Fig. 12. This limit is lower by a

TABLE IV. Results of the fit to a simplified SME test theory prediction. The additional fit parameter is $B_{y,0,\mathrm{syst}} = (1.0 \pm 0.2) \times 10^{-17}$. The errors are statistical.

SME coefficient	Value
$(\tilde{\kappa}_{e-})^{ZZ}$	$(4.8 \pm 1.1) \times 10^{-17}$
$(\tilde{\kappa}_{e-})^{XY}$	$(0.8 \pm 0.4) \times 10^{-17}$
$(\tilde{\kappa}_{e-})^{YZ}$	$(0.0 \pm 0.6) \times 10^{-17}$
$(\tilde{\kappa}_{e-})^{XZ}$	$(-0.3 \pm 0.6) \times 10^{-17}$
$(\tilde{\kappa}_{e-})^{XX} - (\tilde{\kappa}_{e-})^{YY}$	$(0.8 \pm 0.8) \times 10^{-17}$

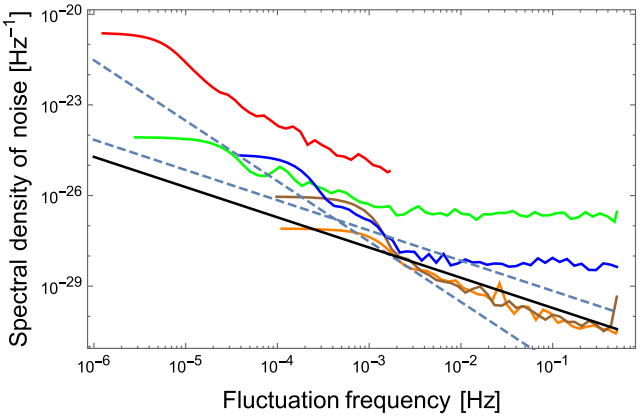

FIG. 12. Power spectral density of normalized cavity frequency fluctuations, referred to a single cavity. Orange: rotating apparatus (this work); brown: nonrotating apparatus (this work). The 95% confidence interval limits of the statistical errors lie 31% below and 81% above the lines. Black: upper limit of the strength of space-time fluctuations with f^{-1} frequency dependence, deduced from this work. Red, green, blue, and blue-gray lines: experimental results and deduced upper limits of particular models, from Ref. [21].

factor 3.7 compared to the previous limit [21], which is shown in Fig. 12 as a dashed line with slope −1.

VI. SUMMARY AND OUTLOOK

In this work, we have demonstrated two main aspects achieved thanks to a significant improvement in the optical setup. First, we increased the sensitivity. This led to statistical uncertainties of the SME coefficients at least two times lower compared to our own previous work and comparable with those in Ref. [11], but with 8 times and 11 times fewer rotations, respectively. The 1σ upper limits for three SME coefficients have been improved, on average, by a factor of 2. Within the RMS model, the present result is a bound to the anisotropy of the speed of light on Earth, $(1/2)|\Delta c(v, \pi/2, 0)|/c < 2.4 \times 10^{-18}$ (1σ limit). This bound represents an improvement by factors of 2.4 and 3.8, compared to Refs. [10,11], respectively. The improvement factors for the SME coefficients and for the RMS coefficient are not directly comparable because of the difference of the models (the RMS fit function is more constrained).

Second, we reduced significantly certain systematic effects, such as tilt, angular rotation speed, and RAM variations. We achieved modulation amplitudes D_y and E_y (related to the fundamental rotation frequency) more than one order smaller than previously. Nevertheless, the time-independent coefficients $D_{y,0}$ and $E_{y,0}$ are still nonzero, and so are $B_{y,0}$ and $C_{y,0}$, relative to their statistical errors. The values of $B_{y,0}$ and $C_{y,0}$ lead to a nonzero value for $(\tilde{\kappa}_{e-})^{ZZ} \simeq 5 \times 10^{-17}$. The improvements in our apparatus led us to rule out tilt variations as a significant source of systematic effects. But since we still observe a (very weak) $4\omega_{\mathrm{rot}}$ signal, which is certainly not a Lorentz violation effect but a systematic, we must conservatively deduce that the values $B_{y,0}$ and $C_{y,0}$ are not a certain signature of Lorentz violation but are also due to systematic effects. These could be due to a deformation of the optical breadboard correlated with rotation angle, caused by the configuration of the rotation table, or due to temperature gradients in the tower housing the experiment.

A few systematic effects (tilt-induced and rotation-speed-induced cavity frequency variation) are sufficiently low to be compatible with future tests of Lorentz invariance aiming at an even higher sensitivity. Substantially longer optical cavities are important toward this goal. Such cavities have been demonstrated by several groups, including our own [22]. An increase in length reduces proportionately the contribution of the mirrors' thermal noise and reduces the total thermal noise. The lower beat frequency instability will allow uncovering systematic effects in a significantly shorter time, which will help to optimize the apparatus more rapidly. In addition, the concomitant smaller cavity line width will also reduce the influence of several systematic disturbances on the beat frequency, e.g., of RAM. The ability to reach an instability of the laser frequency lock to an optical cavity resonance in the low 10^{-17} range [16] is an important foundation for these future efforts.

ACKNOWLEDGMENTS

We thank A. Nevsky and U. Rosowski for important discussions and assistance with the apparatus and D. Iwaschko for the development of electronic subsystems. This work was partially supported by the German Science Foundation DFG (Project No. Schi 431/20-1). We also thank A. Kostelecký and K. Brown for helpful suggestions.

APPENDIX: ANALYSIS IN THE RMS TEST THEORY

1. Introduction

The RMS model [17] has frequently been used in order to interpret experimental tests of Lorentz invariance. Recently, this model has been analyzed in more detail from the point of view of the SME, and it has been found that its application is not permitted under all experimental conditions [23]. We shall not attempt to develop a theoretically correct application but rather will follow the usual analysis procedure and compare the present data with our previous one.

In the RMS model, conventionally, the assumed preferred frame is at rest with respect to the cosmic microwave background (CMB). Nonzero values of three parameters, α, δ, and $\beta - 1/2$, describe modifications of the usual Lorentz transformations. The combination $1/2 - \delta - \beta$ quantifies the directional dependence of the speed of light, and it can be inferred from a comparison of cavity frequencies.

2. Frame definitions

a. Sun-centered celestial equatorial frame

The Sun-centered celestial equatorial frame (SCCEF) with coordinate axes X, Y, Z (Fig. 13) is defined [24,25] as follows:

(i) The center of the frame is located at the center of the Sun.
(ii) The Z axis lies along the Earth rotation axis pointing to the north celestial pole.
(iii) The XY plane coincides with the Earth equatorial plane.

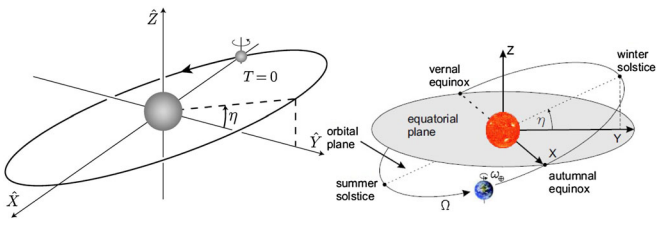

FIG. 13. The SCCEF and the motion of Earth in it, as defined by Kostelecky *et al.* (left) and Eisele *et al.* (right). The definitions agree. Figures are taken from Refs. [24,26].

(iv) The X axis points from the Earth to the Sun, when the Earth is at the vernal equinox (the crossing of the Earth orbit with the XY plane approximately on March 21).
(v) The Y axis is chosen so that a right-handed coordinate system is formed.
(vi) Sidereal time $t_\oplus = 0$ is defined at the time of the vernal equinox.

Note that Herrmann *et al.* [27] use the same definition of the SCCEF. However, from Ref. [28], it appears that the Earth orbital plane is mirrored with respect to the XY plane. This can be seen from Fig. 2.1 of Ref. [28]. The direction of orbital motion remains clockwise when viewed from the north pole looking toward the south pole. Therefore, the Y component of the orbital velocity, Eq. (A6) below, is reversed in the derivations of Herrmann *et al.* compared to the Kostelecky *et al.* definition. This reversal is carried through into the final equations in Table III of Ref. [27].

b. Laboratory frame

The laboratory frame (x, y, z) is defined [26,29] as follows:

(i) The z direction is directed toward the zenith.
(ii) The x and y axes lie in the horizon plane, pointing toward the south and east, respectively.
(iii) The colatitude of the laboratory is denoted by χ.
(iv) The orientation of the laboratory with respect to the SCCEF is determined by the local sidereal time $t_\oplus$.
(v) In the analyses of the experimental data, $t_\oplus = 0$ can be defined by any time the y axis coincides with the Y axis of the SCCEF.

c. Rotations between the SCCEF and laboratory frame

The rotation matrix from the SCCEF to the laboratory frame is given by [29]

$$R^{jJ} = \begin{pmatrix} \cos\chi\cos(\omega_\oplus t_\oplus) & \cos\chi\sin(\omega_\oplus t_\oplus) & -\sin\chi \\ -\sin(\omega_\oplus t_\oplus) & \cos(\omega_\oplus t_\oplus) & 0 \\ \sin\chi\cos(\omega_\oplus t_\oplus) & \sin\chi\sin(\omega_\oplus t_\oplus) & \cos\chi \end{pmatrix}, \tag{A1}$$

where $j = $ x, y, z (laboratory frame) and $J = $ X, Y, Z (SCCEF).

The rotation matrix from the laboratory frame to the SCCEF is the inverse of Eq. (A1),

$$R^{Jj} = \begin{pmatrix} \cos\chi\cos(\omega_\oplus t_\oplus) & -\sin(\omega_\oplus t_\oplus) & \sin\chi\cos(\omega_\oplus t_\oplus) \\ \cos\chi\sin(\omega_\oplus t_\oplus) & \cos(\omega_\oplus t_\oplus) & \sin\chi\sin(\omega_\oplus t_\oplus) \\ -\sin\chi & 0 & \cos\chi \end{pmatrix}. \tag{A2}$$

d. Laboratory velocity

By inspection, the velocity vector $\vec{\beta}_l = \vec{v}_l/c$ of the laboratory with respect to the origin of the SCCEF is given by [29]

$$\vec{\beta}_l = \beta_\oplus \begin{pmatrix} \sin\Omega T \\ -\cos\eta\cos\Omega T \\ -\sin\eta\cos\Omega T \end{pmatrix} + \beta_L \begin{pmatrix} -\sin\omega_\oplus t_\oplus \\ \cos\omega_\oplus t_\oplus \\ 0 \end{pmatrix}, \tag{A3}$$

where $\beta_\oplus$, β_L are defined in Sec. A 2 g. Later, we will neglect the second vector on the rhs.

In contrast, Herrmann [28] and Eisele [26] have opposite signs for the Y component of the first vector on the rhs.

e. CMB rest frame and the Sun velocity toward the CMB

According to Ref. [30], Table 3, the Sun is moving toward the direction given by the galactic coordinates $l =$ 264.4 deg (longitude) and $b = 48.4$ deg (latitude), with speed $v_\odot = 369.5$ km/s [31]. This is converted to right ascension (RA, α) 168 deg, and declination (δ) −7.0 deg [32]. A more accurate value for the latter is −7.22 deg (at time J2000) [33].

Therefore, the velocity of Sun with respect to the CMB is given, in the SCCEF, by the vector

$$v_\odot(\cos\delta\cos\alpha, \cos\delta\sin\alpha, \sin\delta). \tag{A4}$$

The CMB rest frame (Xc, Yc, Zc) is defined as follows:
(i) Xc points toward $(\alpha, \delta) = (167.98, -7.22)$ deg.
(ii) Zc points toward $(\alpha, \delta) = (167.98, 90 - 7.22)$ deg.
(iii) Yc completes a right-handed coordinate system.

A check of Eq. (A4) can be found by noting that in Ref. [29] it is written "for a distant source viewed from Earth at declination δ and right ascension α, the direction of propagation [*of light emitted by the source*] toward the Earth can be written as

$$\hat{p} = \begin{pmatrix} -\cos\delta\cos\alpha \\ -\cos\delta\sin\alpha \\ -\sin\delta \end{pmatrix}."$$

Therefore, the statement that the Sun is moving toward the CMB rest frame in the direction (α, δ) implies that its direction of motion in the SCCEF is

TABLE V. Parameters used.

Name	Symbol	Value
Earth orbital plane tilt with respect to equatorial plane	η	23.4 deg
Laboratory latitude of Düsseldorf	χ	51 deg 11′
CMB rest frame Xc-axis direction, in the SCCEF (right ascension, declination)	α, δ	167.98 deg, −7.22 deg
Orbital boost (Earth orbital speed)	$\beta_\oplus$	$v_\oplus/c = 1.011 \times 10^{-4}$
Laboratory rotational speed due to rotation of Earth only	β_L	$(R_\oplus\omega_\oplus/c)\sin\chi \approx 10^{-6}$
Earth rotation sidereal angular frequency	$\omega_\oplus$	$2\pi/(23\,\mathrm{h}\,56\,\mathrm{m}\,4.09\,\mathrm{s})$
Solar system speed	$v_\odot$	369.5 km/s

$$\hat{p}' = \begin{pmatrix} \cos\delta\cos\alpha \\ \cos\delta\sin\alpha \\ \sin\delta \end{pmatrix}. \tag{A5}$$

Note that both Herrmann and Eisele [26,28] have the Z component of this vector reversed in sign.

Finally, the velocity of the laboratory relative to the CMB, in the SCCEF, is found [26,29] using Eqs. (A3) and (A5),

$$\vec{v} = \beta_\oplus c \begin{pmatrix} \sin\Omega T \\ -\cos\eta\cos\Omega T \\ -\sin\eta\cos\Omega T \end{pmatrix} + \beta_L c \begin{pmatrix} -\sin\omega_\oplus t_\oplus \\ \cos\omega_\oplus t_\oplus \\ 0 \end{pmatrix} + v_\odot \begin{pmatrix} \cos\delta\cos\alpha \\ \cos\delta\sin\alpha \\ \sin\delta \end{pmatrix}.$$

Here, Ω is the angular frequency of Earth's orbital motion. The term proportional to $\beta_L c \simeq v_\oplus = \omega_\oplus R_\oplus \simeq 0.46$ km/s can be neglected. Therefore,

$$\vec{v} \simeq \beta_\oplus c \begin{pmatrix} \sin\Omega T \\ -\cos\eta\cos\Omega T \\ -\sin\eta\cos\Omega T \end{pmatrix} + v_\odot \begin{pmatrix} \cos\delta\cos\alpha \\ \cos\delta\sin\alpha \\ \sin\delta \end{pmatrix}. \tag{A6}$$

f. Cavity vectors in the SCCEF

The vectors describing the orientation of the cavity axes for counterclockwise rotation in the laboratory frame are [26]

$$(\hat{e}_1)_{\mathrm{lab}} = \begin{pmatrix} \cos\omega_{\mathrm{rot}}t \\ \sin\omega_{\mathrm{rot}}t \\ 0 \end{pmatrix}, \qquad (\hat{e}_2)_{\mathrm{lab}} = \begin{pmatrix} \sin\omega_{\mathrm{rot}}t \\ -\cos\omega_{\mathrm{rot}}t \\ 0 \end{pmatrix}.$$

The cavity vectors in the SCCEF are found applying Eq. (A2),

$$\hat{e}_i = R^{Jj}(\hat{e}_i)_{\mathrm{lab}}. \tag{A7}$$

g. Parameters and definitions

Table V summarizes the introduced quantities [34].

3. Derivation of RMS test equation

According to Eq. (6.18) of Ref. [17], the velocity of light is

$$\frac{c}{c(v,\psi)} = 1 + \left(\beta + \delta - \frac{1}{2}\right)\frac{v^2}{c^2}\sin^2\psi + (\alpha - \beta + 1)\frac{v^2}{c^2}, \tag{A8}$$

where v is the speed of the laboratory with respect to the hypothetical preferred frame of reference, ψ is the direction of propagation of the light wave relative to the velocity vector $\vec{v}$, and $c = c(0,0)$.

Taking the inverse and expanding for small violation coefficients, we get

$$\frac{c(v,\psi)}{c} \approx 1 - \left(\beta + \delta - \frac{1}{2}\right)\frac{v^2}{c^2}\sin^2\psi - (\alpha - \beta + 1)\frac{v^2}{c^2}.$$

For two rotating resonators (with time-dependent angles ψ_1 and ψ_2), and assuming that the rate of change in the orientations ψ_i is small, the fractional difference in the speed of light is given as

$$\frac{\Delta c(v,\psi_1,\psi_2)}{c} = \frac{c(v,\psi_1) - c(v,\psi_2)}{c} = -\left(\beta + \delta - \frac{1}{2}\right)\frac{v^2}{c^2}(\sin^2\psi_1 - \sin^2\psi_2).$$

TABLE VI. The coefficients of the (normalized) fit functions of the RMS test theory, Eqs. (A10) and (A11). $t_\oplus$ is the sidereal time, and Ω is the angular frequency of Earth's orbital motion. The location of the experiment is Düsseldorf.

	Numerical expression
$c_{y,0}$	$-0.0305\sin(\Omega t_\oplus) - 0.0091\cos(\Omega t_\oplus) + 0.1871$
$c_{y,1}$	$0.0026\cos(\Omega t_\oplus) - 0.0254$
$c_{y,2}$	$-0.0098\sin(\Omega t_\oplus) + 0.0302\cos(\Omega t_\oplus) + 0.1191$
$c_{y,3}$	$-0.0266\sin(\Omega t_\oplus) - 0.1144\cos(\Omega t_\oplus) + 0.3222$
$c_{y,4}$	$0.1248\sin(\Omega t_\oplus) - 0.0244\cos(\Omega t_\oplus) - 0.7222$
$b_{y,1}$	$0.0126\sin(\Omega t_\oplus) - 0.0387\cos(\Omega t_\oplus) - 0.1529$
$b_{y,2}$	$0.0033\cos(\Omega t_\oplus) - 0.0325$
$b_{y,3}$	$-0.1210\sin(\Omega t_\oplus) + 0.0236\cos(\Omega t_\oplus) + 0.7003$
$b_{y,4}$	$-0.0258\sin(\Omega t_\oplus) - 0.1110\cos(\Omega t_\oplus) + 0.3124$

TABLE VII. Results of RMS test theory analyses. Note: For the second line in the table, the equations of Herrmann *et al.* were multiplied by 2 (for two cavities), and the parameters of Table V were used.

Type of analysis	$-(\beta+\delta-\frac{1}{2})$	$2B_{y,0,\mathrm{syst}}\times(c^2/v_\odot^2)$	$2C_{y,0,\mathrm{syst}}\times(c^2/v_\odot^2)$
Fit functions of Table VI	-7.11×10^{-13}	1.33×10^{-11}	9.48×10^{-12}
	$\pm2.39\times10^{-12}$	$\pm2.14\times10^{-12}$	$\pm2.19\times10^{-12}$
Fit functions given in Ref. [27], modified	-4.67×10^{-13}	1.33×10^{-11}	9.45×10^{-12}
	$\pm2.38\times10^{-12}$	$\pm2.14\times10^{-12}$	$\pm2.20\times10^{-12}$

The change in frequency of a cavity is related to the change of the speed of light by $\Delta\nu/\nu=\Delta c/c$. Then, the RMS test equation is

$$\begin{aligned}\frac{\Delta\nu_1-\Delta\nu_2}{\nu_0}&=-\left(\beta+\delta-\frac{1}{2}\right)\frac{v^2}{c^2}(\sin^2\psi_1-\sin^2\psi_2)\\&=-\left(\beta+\delta-\frac{1}{2}\right)(|\vec{v}\times\vec{e}_1|^2-|\vec{v}\times\vec{e}_2|^2)/c^2\\&=2B_y\sin2\omega_{\mathrm{rot}}t+2C_y\cos2\omega_{\mathrm{rot}}t.\end{aligned}\tag{A9}$$

Note that instead of the cross products one could use a similar expression with scalar products, which simplifies the algebra. The evaluation of this formula gives [using Eq. (A6) for the velocity $\vec{v}$ and Eq. (A7) for the cavity vectors $\hat{e}_i$]

$$2B_y=\left(\beta+\delta-\frac{1}{2}\right)\frac{v_\odot^2}{c^2}(b_{y,1}\sin(\omega_\oplus t_\oplus)+b_{y,2}\cos(\omega_\oplus t_\oplus)+b_{y,3}\sin(2\omega_\oplus t_\oplus)+b_{y,4}\cos(2\omega_\oplus t_\oplus)),\tag{A10}$$

$$2C_y=\left(\beta+\delta-\frac{1}{2}\right)\frac{v_\odot^2}{c^2}(c_{y,0}+c_{y,1}\sin(\omega_\oplus t_\oplus)+c_{y,2}\cos(\omega_\oplus t_\oplus)+c_{y,3}\sin(2\omega_\oplus t_\oplus)+c_{y,4}\cos(2\omega_\oplus t_\oplus)).\tag{A11}$$

Using the parameters of Table V, we obtain the functions displayed in Table VI. Note that in Ref. [11] a rotating resonator is assumed to be compared to a stationary one, and therefore the factor of 2 is missing in the terms of that reference's Table III.

4. Fit results

We analyzed the data of our experiment according to the approaches mentioned above. Two additional fit coefficients, $2B_{y,0,\mathrm{syst}}$ and $2C_{y,0,\mathrm{syst}}$, were added to the rhs of Eqs. (A10) and (A11), respectively, in order to describe systematic effects. The results are given in Table VII. We see that the values of the violation coefficient $\beta+\delta-1/2$ are compatible with zero. The fit errors are nearly equal in the two cases. They are a factor of 2.4 smaller than our previous result.

[1] A. Kostelecký and N. Russell, Data tables for Lorentz and CPT violation, Rev. Mod. Phys. **83**, 11 (2011).
[2] T. Pruttivarasin, M. Ramm, S. Porsev, I. Tupitsyn, M. Safronova, M. Hohensee, and H. Häffner, Michelson-Morley analogue for electrons using trapped ions to test Lorentz symmetry, Nature (London) **517**, 592 (2015).
[3] P. L. Stanwix, M. E. Tobar, P. Wolf, C. R. Locke, and E. N. Ivanov, Improved test of Lorentz invariance in electrodynamics using rotating cryogenic sapphire oscillators, Phys. Rev. D **74**, 081101 (2006).
[4] A. Brillet and J. L. Hall, *Laser Spectroscopy IV* (Springer, Berlin Heidelberg, 1979), pp. 12–20.
[5] C. Braxmaier, H. Müller, O. Pradl, J. Mlynek, A. Peters, and S. Schiller, Test of Relativity using a Cryogenic Optical Resonator, Phys. Rev. Lett. **88**, 010401 (2002).
[6] H. Müller, S. Herrmann, C. Braxmaier, S. Schiller, and A. Peters, Modern Michelson-Morley Experiment using Cryogenic Optical Resonators, Phys. Rev. Lett. **91**, 020401 (2003).
[7] P. Antonini, M. Okhapkin, E. Göklü, and S. Schiller, Test of constancy of speed of light with rotating cryogenic optical resonators, Phys. Rev. A **71**, 050101(R) (2005).
[8] S. Herrmann, A. Senger, E. Kovalchuk, H. Müller, and A. Peters, Test of the Isotropy of the Speed of Light using a

Continuously Rotating Optical Resonator, Phys. Rev. Lett. **95**, 150401 (2005).

[9] C. Eisele, M. Okhapkin, A. Y. Nevsky, and S. Schiller, A crossed optical cavities apparatus for a precision test of the isotropy of light propagation, Opt. Commun. **281**, 1189 (2008).

[10] C. Eisele, A. Nevsky, and S. Schiller, A Laboratory Test of the Isotropy of Light Propagation at the 10^{-17} Level, Phys. Rev. Lett. **103**, 090401 (2009).

[11] S. Herrmann, A. Senger, K. Möhle, M. Nagel, E. Kovalchuk, and A. Peters, Rotating optical cavity experiment testing lorentz invariance at the 10^{-17} level, Phys. Rev. D **80**, 105011 (2009).

[12] H. Müller, S. Herrmann, A. Saenz, A. Peters, and C. Lämmerzahl, Optical cavity tests of Lorentz invariance for the electron, Phys. Rev. D **68**, 116006 (2003).

[13] H. Müller, P. L. Stanwix, M. E. Tobar, E. Ivanov, P. Wolf, S. Herrmann, A. Senger, E. Kovalchuk, and A. Peters, Tests of Relativity by Complementary Rotating Michelson-Morley Experiments, Phys. Rev. Lett. **99**, 050401 (2007).

[14] G. Amelino-Camelia, Quantum-spacetime phenomenology, Living Rev. Relativity **16**, 5 (2013).

[15] T. Legero, T. Kessler, and U. Sterr, Tuning the thermal expansion properties of optical reference cavities with fused silica mirrors, J. Opt. Soc. Am. B **27**, 914 (2010).

[16] Q. F. Chen, A. Nevsky, and S. Schiller, Locking the frequency of lasers to an optical cavity at the 1.6×10^{-17} relative instability level, Appl. Phys. B **107**, 679 (2012).

[17] R. Mansouri and R. U. Sexl, A test theory of special relativity: I. Simultaneity and clock synchronization, Gen. Relativ. Gravit. **8**, 497 (1977).

[18] V. A. Kostelecký and M. Mewes, Signals for Lorentz violation in electrodynamics, Phys. Rev. D **66**, 056005 (2002).

[19] D. M. Palmer, A fast chi-squared technique for period search of irregularly sampled data, Astrophys. J. **695**, 496 (2009).

[20] F. R. Klinkhamer and M. Risse, Addendum: Ultrahigh-energy cosmic-ray bounds on nonbirefringent modified maxwell theory, Phys. Rev. D **77**, 117901 (2008).

[21] S. Schiller, C. Lämmerzahl, H. Müller, C. Braxmaier, S. Herrmann, and A. Peters, Experimental limits for low-frequency space-time fluctuations from ultrastable optical resonators, Phys. Rev. D **69**, 027504 (2004).

[22] Q.-F. Chen, A. Nevsky, M. Cardace, S. Schiller, T. Legero, S. Häfner, A. Uhde, and U. Sterr, A compact, robust, and transportable ultra-stable laser with a fractional frequency instability of 1×10^{-15}, Rev. Sci. Instrum. **85**, 113107 (2014).

[23] V. A. Kostelecký and M. Mewes, Fermions with Lorentz-violating operators of arbitrary dimension, Phys. Rev. D **88**, 096006 (2013).

[24] R. Bluhm, V. A. Kostelecký, C. D. Lane, and N. Russell, Probing Lorentz and CPT violation with space-based experiments, Phys. Rev. D **68**, 125008 (2003).

[25] V. A. Kostelecký and M. Mewes, Electrodynamics with Lorentz-violating operators of arbitrary dimension, Phys. Rev. D **80**, 015020 (2009).

[26] C. Eisele, Ph.D. Thesis, Heinrich-Heine-Universität Düsseldorf, 2009.

[27] S. Herrmann, A. Senger, K. Moehle, M. Nagel, E. V. Kovalchuk, and A. Peters, Rotating optical cavity experiment testing Lorentz invariance at the 10^{-17} level, Phys. Rev. D **80**, 105011 (2009).

[28] S. Herrmann, Ph.D. Thesis, Humboldt-Universität zu Berlin, 2006.

[29] V. A. Kostelecký and M. Mewes, Cosmological Constraints on Lorentz Violation in Electrodynamics, Phys. Rev. Lett. **87**, 251304 (2001).

[30] A. Kogut, C. Lineweaver, G. F. Smoot, C. L. Bennett, A. Banday, N. W. Boggess, E. S. Cheng, G. Deamici, D. J. Fixsen, G. Hinshaw, P. D. Jackson, M. Janssen, P. Keegstra, K. Loewenstein, P. Lubin, J. C. Mather, L. Tenorio, R. Weiss, D. T. Wilkinson, and E. L. Wright, Dipole anisotropy in the COBE differential microwave radiometers 1st-year sky maps, Astrophys. J. **419**, 1 (1993).

[31] "Toward" is the implied meaning, since in the abstract the galactic coordinates are mentioned with the word "toward."

[32] Using the calculator http://www.robertmartinayers.org/tools/coordinates.html.

[33] C. H. Lineweaver, L. Tenorio, G. F. Smoot, P. Keegstra, A. J. Banday, and P. Lubin, The dipole observed in the COBE DMR four-year data, Astrophys. J. **470**, 38 (1996).

[34] In Ref. [27], a different value for the declination δ is given in its text and in its Table III caption. We do not know how this issue and the factor 2 mentioned further below influenced its final results.